

A New Automatic Fault Diagnosis Algorithm for Electrical Equipment Based on Infrared Thermography

Nguyen Xuan Truong¹, Nguyen Thai Hoc^{2*}, Ngo Tri Duong² & Dao Xuan Tien¹

Faculty of Engineering, Vietnam National University of Agriculture, Hanoi 12400, Vietnam

Abstract

In this paper, a novel algorithm is proposed for an Efficient Fault Diagnosis Method (EFDM) for electrical equipment in real time. A combined optical and thermal image processing system is employed to detect thermal anomalies in electrical components in real time. A video camera is initially used to monitor and identify the electrical components, while an infrared camera, aligned with the same viewpoint, is used to capture thermal images of the equipment. The EFDM is then applied to identify and locate faults in electrical components. Numerical results indicate that the proposed algorithm achieves higher accuracy in detecting thermal anomalies compared to existing methods. Evaluation across 300 scenarios shows that the proposed method achieves 97.57% accuracy in localizing abnormal electrical components and 95.30% accuracy in estimating their surface temperatures. These results demonstrate that the proposed thermal anomaly detection algorithm is effective for electrical power monitoring applications.

Keywords

Thermal imaging, thermal image segmentation, thermal anomalies detection, power monitoring system, electrical equipment

Introduction

It is known that the temperature of working electrical components raise due to Joule heating as flowing equation:

$$Q = I^2 R t \quad (1)$$

where, I is the electrical current flows through a resistivity components having resistance R . Therefore, the main reasons to increase the heat of these electrical components are high current flow (overloading) or increased resistance due to factors such as poor connections, load imbalance, or wiring errors (Fatima *et al.*, 2025). Overheating in these components can result in failure or damage to the power distribution system (Market *et al.*, 2025). Consequently, a

Received: April 10, 2025
Accepted: June 26, 2025

Correspondence to
Nguyen Thai Hoc
nguyenthaihoc@vnua.edu.vn

key challenge in modern electrical monitoring systems is the real-time detection of abnormal electrical components (Ahmed *et al.*, 2015; Baba *et al.*, 2022; Balakrishnan *et al.*, 2022; Huda & Taib, 2013; Amit *et al.*, 2024).

Traditional methods detect faults mainly under high load and with clear line-of-sight thermal imaging (McIntosh & Huff, 2016). This study overcomes the limitation of relying solely on surface temperature by integrating infrared thermography with structured risk assessment—considering failure modes, stressors, and risk severity. The proposed framework enhances maintenance decisions and safety, offering better detection of latent faults. However, it requires contextual data and cannot capture internal contact temperatures.

This method distinguishes itself by incorporating thermal data into a comprehensive diagnostic and predictive maintenance framework, rather than relying solely on radiometric values. Nonetheless, its effectiveness is constrained by thermal contrast dependence, lack of temporal dynamics, and sensitivity to environmental noise—factors that may cause false hotspot detection.

Elevated temperatures in electrical components can degrade power system reliability. Infrared thermography, as noted by Shariff *et al.* (2019), is a key technique for early fault diagnosis through detection of thermal anomalies. According to Kregg (2004), infrared thermography (IR) was applied as a preventive maintenance tool to monitor equipment integrity in substations. By detecting thermal anomalies, IR enabled early fault identification in components like transformers and circuit breakers, outperforming traditional methods such as DGA, ultrasonic, and visual inspections—detecting over 50% of issues. However, IR requires complementary tests for accurate diagnosis and maintenance planning. Its key roles in power system monitoring are outlined below.

Early fault detection of electrical equipment

Infrared thermography is recognized as an effective non-destructive technique for monitoring electrical asset temperatures (Kornkanok *et al.*, 2024). Jaffery & Dubey (2014) proposed a novel method analyzing hotspot locations and temperature change rates

for early fault detection. Their systems—NIOLVIS and NIRTVMS—demonstrated non-invasive, accurate, and reliable performance, outperforming conventional monitoring approaches. To enhance fault diagnosis in electrical components, various intelligent systems have been developed (Zou & Huang, 2015; Jadin & Taib, 2012). These systems typically follow four steps: (i) infrared image acquisition, (ii) region of interest (ROI) identification, (iii) feature extraction, and (iv) condition classification of electrical equipment.

Fire prevention

On operating conditions, the temperature of the electrical equipment depends on many influencing factors such as over-voltage, high current, unbalance loading, poor connections or cracks in insulation, etc (Coutin *et al.*, 2012). The overheating of these electrical components may cause malfunctions or even fires to break out. It is important for early prevention temperature monitoring. Therefore, many researchers try to detect and early revert thermal abnormalities in electrical components early on based on infrared thermography (Huda & Taib, 2013, Bagavathiappan *et al.*, 2013, Xia, *et al.*, 2021). Huda & Taib (2013) employed a multilayer perceptron (MLP) neural network with statistical features to assess thermal conditions of electrical equipment. A component was classified as defective if its maximum temperature exceeded the reference value by more than 5 °C. Compared to discriminant analysis, the MLP achieved higher accuracy at 82.4%.

Energy saving and prolonging the lifetime

Overheating significantly shortens the lifespan of electrical components, making early thermal detection via infrared thermography an effective preventive measure. Sedighi *et al.* (2020) estimated the lifetime of distribution transformers by extracting body temperature from infrared images. The results showed high consistency with oil test-based estimations, with a lifetime prediction error below 10%.

To address existing limitations, this study introduces a spatial-temporal modeling algorithm for infrared-based fault diagnosis in residential electrical systems. By analyzing infrared image sequences, the method captures both spatial and temporal pixel features, reducing

false hotspot detection and improving diagnostic accuracy under real-world conditions. The approach enhances the robustness and early-warning capability of thermal monitoring systems by bridging static image analysis with dynamic modeling. Integrating image processing and machine learning, the study advances the development of intelligent electrical monitoring solutions. The main contributions of this study are: (i) A novel Optimal Threshold Segmentation (OTS) algorithm that improves the classical Otsu method by iteratively minimizing within-class variance, effectively addressing over-segmentation in noisy, low-contrast thermal images; (ii) A spatial-temporal modeling technique for analyzing infrared image sequences to detect dynamic hotspot behavior and reduce false detections from ambient or reflected radiation; (iii) A real-time intelligent fault detection framework integrating segmentation, thermal feature extraction, and temporal analysis to classify thermal states into three priority levels with maintenance recommendations; and (iv) Experimental validation on 300 real infrared images, achieving 97.57% segmentation precision and 95.3% temperature estimation accuracy—outperforming conventional Otsu-based methods and confirming applicability in smart power monitoring systems.

Materials and Methods

The block diagram of the proposed method for electrical equipment defect detection is illustrated in **Figure 1**. There are 3 stages in total: Image processing, temperature segmentation, and image feature analysis. The details of these stages are described in this section.

Otsu’s threshold algorithm

Let us assume that a given infrared image which needs to be segmented the high-temperature electrical components and the ground regions has L grey levels. Let $\{n_i, i = 1, \dots, L\}$ denote the number of pixels at level, and then the total number of pixels of the given infrared image is $M \times N$. It is computed in equation (2).

$$\sum_{i=1}^L n_i = M \times N \tag{2}$$

where M is the width and N is the height of the given infrared image, respectively. We assume that the grey level histogram of the given infrared image is normalized. The probability distribution is computed in equation (3).

$$p_i = \frac{n_i}{M \times N} \tag{3}$$

where

$$\begin{cases} 0 \leq p_i \leq 1 \\ \sum_{i=1}^L p_i = 1 \end{cases} \tag{4}$$

Let $I(x, y)$ denote the grey value of a pixel at location $(x, y), \{0 \leq x < M, 0 \leq y < N\}$ and T denotes the threshold value of the Otsu’s method (Otsu, 1979)). The binary segmentation $\alpha(x, y)$ of the given infrared image then is obtained by comparing the grey value of each pixel with this threshold T , and it is split into two classes namely C_0, C_1 . C_1 denotes the class, which includes all the pixels having a grey value higher than T . These pixels belong to grey levels

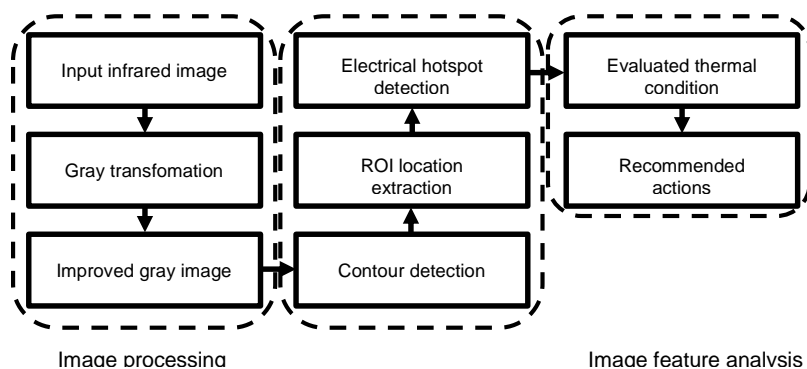


Figure 1. Block diagram of the proposed FEDM method

$[T+1, T+2, \dots, L]$. While C_1 denotes the class, which includes all the pixels having a grey value less than T . These pixels belong to grey levels $[1, 2, \dots, T]$. The binary segmentation image is given in equation (5).

$$\alpha(x, y) = \begin{cases} 1 & \text{if } I(x, y) > T; \text{ Class } C_0 \\ 0 & \text{otherwise; Class } C_1 \end{cases} \quad (5)$$

Let $\mu_0(T)$ and $\mu_1(T)$ denote the mean pixel grey value, $\omega_0(T)$, and $\omega_1(T)$ denote the weight parameter, $\sigma_0^2(T)$, and $\sigma_1^2(T)$ denote the variances of classes C_0, C_1 , respectively. They are given in equation (6), and equation (7).

$$\begin{cases} \omega_0(T) = \sum_{i=1}^T p_i \\ \mu_0(T) = \frac{\sum_{i=1}^T ip_i}{\omega_0(T)} \\ \sigma_0^2(T) = \sum_{i=1}^T (i - \mu_0(T))^2 \frac{p_i}{\omega_0(T)} \end{cases} \quad (6)$$

$$\begin{cases} \omega_1(T) = \sum_{i=T+1}^L p_i \\ \mu_1(T) = \frac{\sum_{i=T+1}^L ip_i}{\omega_1(T)} \\ \sigma_1^2(T) = \sum_{i=T+1}^L (i - \mu_1(T))^2 \frac{p_i}{\omega_1(T)} \end{cases} \quad (7)$$

The mean grey level of all pixels in the infrared image is computed in equation (8).

$$\mu = \frac{\sum_{i=0}^L ip_i}{\sum_{i=0}^L p_i} = \frac{\sum_{i=0}^L ip_i}{1} = \omega_0(T)\mu_0(T) + \omega_1(T)\mu_1(T) \quad (8)$$

The between-class variance is computed in equation (9).

$$\sigma_b^2(T) = \omega_0(T)(\mu_0(T) - \mu)^2 + \omega_1(T)(\mu_1(T) - \mu)^2 \quad (9)$$

The within-class variance is computed in equation (10).

The optimal threshold T^* value of the Otsu's method is determined as given in equation (11) or in equation (12).

$$T^* = \arg \max_{1 \leq T < L} \{ \sigma_b^2(T) \} \quad (11)$$

$$T^* = \arg \min_{1 \leq T < L} \{ \sigma_w^2(T) \} \quad (12)$$

Unfortunately, the original Otsu's method may fail or not perform well enough if there is a significant difference in intra-class variance (Zhou & Xia, 2016). It is proven that the threshold of Otsu's method is near to pixel class with high intracranial variance (Xu, 2011). It means that the threshold of the Otsu segmentation method may lead to over-segmentation problems with noisy images or those images of low contrast and not well-distributed pixel density. Therefore, in the next section, we try to construct an effective threshold-adjusting strategy for infrared image segmentation based on the Otsu's method.

Proposed infrared image segmentation algorithm

Property: Let T^* be the optimal threshold, which divides a given infrared image into two classes with the smallest within-class variance in each class. $\mu_0(T^*)$, and $\mu_1(T^*)$ are the mean pixel grey values with T^* . If $T_m = 0.5[\mu_0(T^*) + \mu_1(T^*)]$, then $T^* = T_m$ or there are no pixels having grey value in the range between T^* and T_m .

Proof: Let T^* represent the optimal threshold, which minimizes the within-class variance in each class. $\sigma_w^2(T) \geq \sigma_w^2(T^*), \forall T \in [1, \dots, L]$. We assume that $T^* \leq T_m$ therefore

$$\sum_{i=T^*+1}^{T_m} (i - \mu_1(T^*))^2 p_i \geq \sum_{i=T^*+1}^{T_m} (i - \mu_0(T_m))^2 p_i \quad (13)$$

The within-class variance is computed as given in equation (14).

$$\sigma_w^2(T^*) = \omega_0(T^*) \sum_{i=1}^{T^*} (i - \mu_0(T^*))^2 \frac{p_i}{\omega_0(T^*)} + \omega_1(T^*) \sum_{i=T^*+1}^L (i - \mu_1(T^*))^2 \frac{p_i}{\omega_1(T^*)} \quad (14)$$

↔

$$\sigma_w^2(T^*) = \sum_{i=1}^{T^*} (i - \mu_0(T^*))^2 p_i + \sum_{i=T^*+1}^L (i - \mu_1(T^*))^2 p_i \quad (15)$$

$$= \sum_{i=1}^{T^*} (i - \mu_0(T^*))^2 p_i + \sum_{i=T^*+1}^{T_m} (i - \mu_1(T^*))^2 p_i + \sum_{i=T_m+1}^L (i - \mu_1(T^*))^2 p_i \quad (16)$$

According to equation (13), we have:

$$\sigma_w^2(T_m) \geq \sum_{i=1}^{T_m} (i - \mu_0(T_m))^2 p_i + \sum_{i=T_m+1}^{T_m} (i - \mu_0(T_m))^2 p_i + \sum_{i=T_m+1}^L (i - \mu_1(T_m))^2 p_i \quad (17)$$

or

$$\Leftrightarrow \sigma_w^2(T_m) \geq \sum_{i=1}^{T_m} (i - \mu_0(T_m))^2 p_i + \sum_{i=T_m+1}^L (i - \mu_1(T_m))^2 p_i \quad (18)$$

$$\sigma_w^2(T^*) \geq \sigma_w^2(T_m) \Leftrightarrow T^* \equiv T_m \text{ or } \sum_{i=T_m}^{T^*} p_i = 0 \quad (19)$$

By a similar method, it can be proved that

$$T^* \equiv T_m \text{ or } \sum_{i=T_m}^{T^*} p_i = 0 \text{ in the case of } T^* > T_m.$$

Based on the above analysis, an infrared image segmentation algorithm based on the improved Otsu algorithm is called the Optimal Threshold Segmentation (OTS) algorithm. In this proposed algorithm, an optimal threshold T^* can be calculated iteratively. The details of our proposed OTS algorithm are described in Algorithm 1.

Algorithm 1 OTS algorithm

Input:

Raw infrared image $I(x, y)$;

A grey level histogram $hist$.

Output:

Optimal thresholds of each infrared image T^* ;

Segmentation images $\alpha(x, y)$.

Initiation: The predefined threshold θ_0^* ;

Choose an initial threshold $T_0 = 1$, which divides a given infrared image into two classes; $d = \infty$;

Procedure OTS_ALGORITHM($\theta_0^*, T_0, d, T^*, \alpha(x, y)$)

- 1 $\theta_0^*, T_0, d, T^*, \alpha(x, y)$
- 2 Chose the optimal threshold: $T^* = T_0$;
- 3 **while** $d > \theta_0^*$ **do**
 Calculate the mean pixel grey value with threshold $T^* : \mu_0(T^*)$, and $\mu_1(T^*)$ by using equations (6), (7).
 Calculate the mean level of two classes.
- 5 $T_m = 0.5 \lfloor \mu_0(T^*) + \mu_1(T^*) \rfloor \quad (20)$

Calculated the distance between the threshold value and the mean level of two classes:

$$d = |T^* - T_m| \quad (21)$$

7 **if** $d > \theta_0^*$ **then** $T^* = T^* + 1$.

8 **end if**

9 **end while**

10 The optimal threshold of the candidate infrared image is T^* .

The binary segmentation image is obtained by using the following

11 equation:

$$\alpha(x, y) = \begin{cases} 1 & \text{if } I(x, y) > T^*; \text{Class } C_0 \\ 0 & \text{otherwise; Class } C_1 \end{cases} \quad (22)$$

12 **end procedure**

Electrical hotspot detection

In this section, the hotspots of electrical components and the hot regions of an image with pixel intensity greater than a threshold are detected automatically. From equation (22), the defect electrical components contained in the thermal image are given in equation (23).

$$\beta(x, y) = \begin{cases} I(x, y) & \text{if } \alpha(x, y) = 1 \\ 0 & \text{if } \alpha(x, y) = 0 \end{cases} \quad (23)$$

The temperature of each defective electrical component at each pixel in location is computed as given in equation (24).

$$T(x, y) = T_{\min} + \frac{\beta(x, y)}{255} (T_{\max} - T_{\min}) \quad (24)$$

where T_{\max}, T_{\min} denote the highest and lowest temperature extract from an infrared image, respectively. Unfortunately, the total amount of electromagnetic energy received by a thermal camera, which influences the temperature measurement by infrared thermography, is based on Stefan-Boltzmann's law. It is a combination of the energy emitted by the object, the reflected energy, and the energy emitted from the ambient temperature (Doshvarpassand *et al.*, 2019), and may lead to some fake hotspots on the infrared image. Therefore, it is important to minimize the amount of these fake hotspots. To do this, the pixel characteristic types corresponding to spatial and

temporal information should be considered carefully (Luo *et al.*, 2019). In this study, a spatial-temporal modeling algorithm for electrical hotspot detection is proposed. Our proposed algorithm detects the defective electrical component from infrared image sequences.

Let $I(x, y, j)$ denote the grey value of a pixel at location $(x, y) \{0 \leq x < M; 0 \leq y < N\}$ at the $j^{th} \{0 < j \leq k\}$ frame of infrared image sequence. The segmented image at frame k^{th} is computed as given in equation (25).

$$\bar{\beta}(x, y, k) = \frac{1}{k} \sum_{x=0}^M \sum_{y=0}^N \sum_{j=0}^k \beta(x, y, j) \quad (25)$$

The temperature of the electrical component in equation (24) is rewritten as given in equation (26).

$$T(x, y, k) = T_{\min} + \frac{\bar{\beta}(x, y, k)}{255} (T_{\max} - T_{\min}) \quad (26)$$

$0 \leq x < M$
 $0 \leq y < N$

where $T(x, y, k)$ is the temperature of pixel at location (x, y) at frame k^{th} . The process of infrared image segmentation is depicted in **Figure 2**.

Let $T(x, y, 0)$ denote the temperature of a pixel at location (x, y) when the electrical equipment works in a normal condition. It is called the reference temperature of the candidate pixel. The temperature values of pixels $T(x, y, 0), \{\forall x \in [0, M); y \in [0, N)\}$ are obtained by manual measurement. The difference in temperature values of the same position pixel between two working conditions $\Delta T; \Delta T_1$ is used to detect defective electrical equipment. Due to the value of $\Delta T, \Delta T_1$, the working conditions of electrical equipment are classified into two classes: normal and defective (overheated)

classes. These values are computed in equations (27), (28) and given in **Table 1**.

$$\Delta T = |T(x, y, k) - T(x, y, 0)| \quad (27)$$

$$\Delta T_1 = \left| T(x, y, k) - \frac{1}{k} \sum_{i=1}^k T(x, y, i) \right| \quad (28)$$

Experiment and analysis

To evaluate the real-time performance of the proposed FFDM method, an experimental setup for electrical equipment defect detection was conducted as described below.

Image acquisition system

The thermal images of electrical equipment are taken by an infrared camera at different view angles. In this study, a FLIR E8-XT thermal camera was used to capture the images. **Table 2** shows the specifications of FLIR E8-XT. For capturing the infrared image of electrical equipment, the distance between the infrared camera and the electrical equipment varies from 0.5 to 2.5 meters. The ambient temperature of the electrical equipment is between $28^\circ C$ and $32^\circ C$ during the experimental conduction.

Evaluating indicator

In this section, the performance of our proposed scheme in terms of infrared image segmentation and electrical hotspot detection is presented.

For the first quality indicator, the quality of the segmented defective electrical equipment region can be measured by comparing manual segmentation to our proposed segmented algorithm. Let TP denote the true positive in which pixels of defective electrical equipment areas are classified correctly as defective electrical equipment pixels; FP (False positive):

Table 1. The classification of electrical equipment due to its thermal condition

| The difference in temperature ($^\circ C$) | Priority level | Thermal condition | Recommended actions |
|-------------------------------------------------------|----------------|-------------------|------------------------------------------------------------------------------|
| $\Delta T \leq 5$ or $\Delta T_1 \leq 5$ | I | Normal | Small overheating and need further study |
| $5 < \Delta T \leq 15$ or $5 < \Delta T_1 \leq 15$ | II | Overheated | Some potential defect locations and need to repair as soon as possible |
| $15 \leq \Delta T$ or $15 \leq \Delta T_1$ | III | Overheated | Thermal defects in electrical equipment and it must be corrected immediately |

Table 2. Technical specifications of thermal camera

| Parameters | FLIR E8-XT | Unit |
|-------------------------|-------------|--------|
| Resolution | 320 x 240 | Pixels |
| Measurement method | Radiometric | |
| Measurement range | -20 to +250 | (°C) |
| Accuracy | ±2 | (°C) |
| Temperature sensitivity | 0.05 | (°C) |
| Spectral range | 7.5 to 13 | (μm) |

Pixels in non-defective electrical equipment areas are misclassified as defective electrical equipment pixels; *TN* (True negative): pixels in non-defective electrical equipment areas are classified correctly as non-defective electrical equipment pixels; *FN* (False negative) pixels of defective electrical equipment are misclassified as non-defective electrical equipment pixels.

Precision (P_r), Recall (R_c), and (F_1) score are calculated as given in Equations (29), (30), (31), respectively.

$$P_r = \frac{TP}{TP + FP} \times 100 \tag{29}$$

$$R_c = \frac{TP}{TP + FN} \times 100 \tag{30}$$

$$F_1 = \frac{2 \times P_r \times R_c}{P_r + R_c} \tag{31}$$

For the second quality indicator, the highest temperature values of the defective electrical components are extracted automatically from our proposed algorithm. They are compared with the temperature values which are measured manually by a digital thermometer at the same time and the same location of the electrical components.

Results and Discussion

Segmentation results

In this paper, 300 thermal images of several kinds of electrical equipment, such as power transformers, high-voltage lines, electrical motors, and circuit main boards, are used to detect the location of abnormal electrical components. In **Figure 3**, the segmentation results of these thermal images are shown. The first column (**Figure 3a**) depicted the original

thermal images. The ground truth of segmentation images is given in the second column (**Figure 3b**). The segmented images of the defect electrical components obtained by Otsu's threshold algorithm and our proposed OTS algorithm are depicted in the third fourth columns, respectively (**Figures 3c, 3d**). The comparison of thermal image segmentation results between the Otsu's threshold algorithm and our proposed OTS algorithm are given in **Table 3**. **Table 3** shows the image segmentation results with three indicators: Precision, Recall, and score of each algorithm on the same image samples. As defined in formulas (29), (30), and (31) these indicators represent the correct classification ratio of the algorithm. Therefore, the higher value of these indicators indicates the better performance of the algorithm. The simulation results in **Table 3** show that our proposed method outperforms the Otsu's threshold algorithm on all image samples. The averages of our proposed OTS algorithm are 97.57%, 96.54% and 97.05%, respectively. These values obtained by Otsu's threshold algorithm were only 96.31%, 93.11% and 94.68%, respectively. Our proposed OTS algorithm demonstrates strong performance for image-processing applications.

Temperature extraction results

Figure 4 shows the temperature extraction results from thermal images of electrical equipment. **Figure 4a** depicts the temperature extraction from the power transmission line; The **Figures 4b, 4c, 4d, 4e** and **4f** show the results of hotspot detection on the electrical switchboard, the electronic circuit, the electrical motor, and the power transformer, respectively. **Table 4** shows

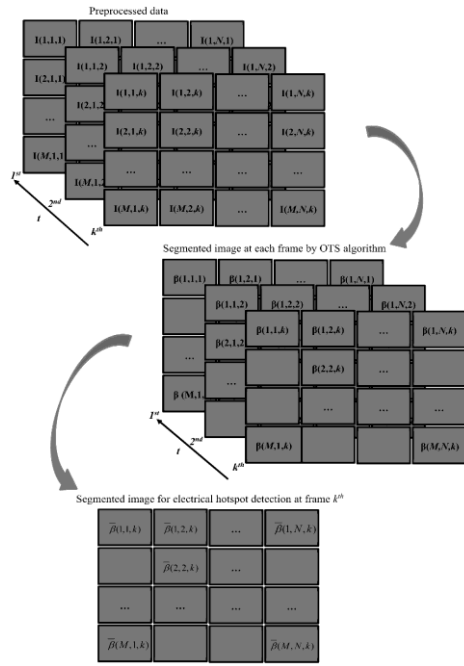


Figure 2. The process of infrared image segmentation

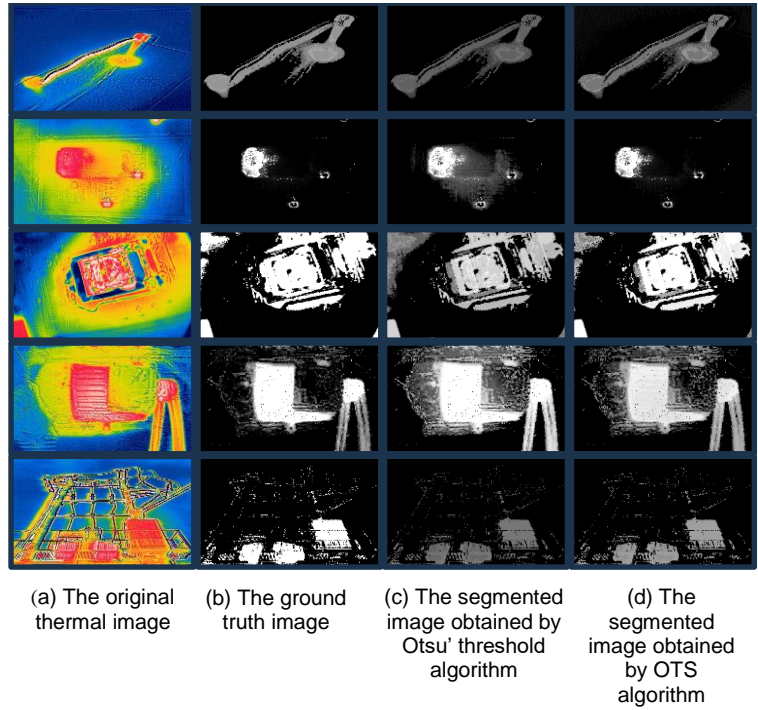


Figure 3. The process of defect detection in electrical equipment

Table 3. The comparison of thermal image segmentation results between the Otsu' threshold algorithm and our proposed OTS algorithm

| Sample | Otsu | | | OTS | | |
|---------|-----------|-----------|-----------|-----------|-----------|-----------|
| | <i>Pr</i> | <i>Rc</i> | <i>F1</i> | <i>Pr</i> | <i>Rc</i> | <i>R1</i> |
| 1 | 96.72 | 95.10 | 95.90 | 97.39 | 95.64 | 96.51 |
| 2 | 95.95 | 91.03 | 93.42 | 97.52 | 96.39 | 96.95 |
| 3 | 96.22 | 91.63 | 93.87 | 97.65 | 96.52 | 97.08 |
| 4 | 95.66 | 89.47 | 92.46 | 97.79 | 97.03 | 97.41 |
| 5 | 95.24 | 88.61 | 91.80 | 97.92 | 97.80 | 97.86 |
| 6 | 95.81 | 91.12 | 93.40 | 97.66 | 97.28 | 97.47 |
| 7 | 96.15 | 93.43 | 94.77 | 97.53 | 97.02 | 97.27 |
| 8 | 96.13 | 92.90 | 94.49 | 97.65 | 96.26 | 96.95 |
| 9 | 96.30 | 94.06 | 95.16 | 97.77 | 95.39 | 96.57 |
| 10 | 96.08 | 91.27 | 93.61 | 97.63 | 94.76 | 96.18 |
| 11 | 96.35 | 91.76 | 94.00 | 97.76 | 94.89 | 96.31 |
| 12 | 96.37 | 92.40 | 94.34 | 98.04 | 96.03 | 97.02 |
| 13 | 96.51 | 92.53 | 94.47 | 97.91 | 95.90 | 96.89 |
| 14 | 96.29 | 93.56 | 94.90 | 98.04 | 96.78 | 97.41 |
| 15 | 96.55 | 93.69 | 95.09 | 98.05 | 97.16 | 97.61 |
| 16 | 96.58 | 94.47 | 95.52 | 97.14 | 96.13 | 96.63 |
| 17 | 96.44 | 94.33 | 95.37 | 96.74 | 95.99 | 96.37 |
| 18 | 96.85 | 96.73 | 96.79 | 96.90 | 97.53 | 97.21 |
| 19 | 96.98 | 96.85 | 96.91 | 97.18 | 97.55 | 97.37 |
| 20 | 97.11 | 97.37 | 97.24 | 97.06 | 98.70 | 97.87 |
| Average | 96.31 | 93.11 | 94.68 | 97.57 | 96.54 | 97.05 |

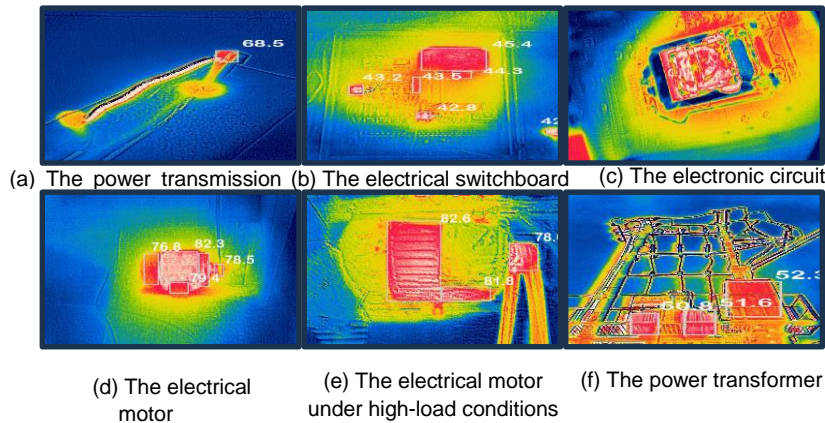


Figure 4. Extracting temperature values of electrical components

the simulation results of extracting temperature from the IR image. The comparison between the ground truth (the measured temperature) that was obtained by manual manner and the extracted temperature obtained by our proposed method shows that the average accuracy is 0.951. The highest and smallest difference in temperature between the measured temperature and the extracted temperature are $3.8(^{\circ}C)$ and $1.6(^{\circ}C)$, respectively. For evaluation, we conducted additional experiments on a public thermal dataset (Doutorado, 2023) to measure the performance of our proposed method.

Temperature extraction results

The RNA_Eduardo_Tese model offers a versatile, AI-based solution for monitoring and maintaining electrical infrastructure. It enables autonomous identification of power equipment such as transformers and voltage switches, facilitating predictive maintenance, and enhancing grid reliability. When integrated with drone platforms, the model supports real-time aerial surveillance of power lines, enabling rapid detection of faults and reducing transmission downtime. In post-disaster scenarios, it assists in damage assessment and prioritization of restoration tasks. Moreover, the model contributes to infrastructure planning by classifying equipment types and supporting optimized layout designs, while also improving asset inventory control by detecting aging or obsolete components requiring replacement. **Figure 5** shows the temperature estimation on thermal image dataset (Doutorado, 2023). The

RGB and thermal images of the hottest parts of the transformer are depicted in **Figures 5a, 5b**, while the extracted temperature of the hotspots are shown in **Figure 5c**. **Figure 6** shows the difference between measured and extracted temperature. As described in Figures 5 and 6, there is no significant difference between the measured and extracted temperature values (δT). Greater than 92% of the measured points have a difference in temperature between the measured and extracted temperature values less than 5 Celsius degree.

To validate the real-time performance of the proposed thermal image analysis model for power equipment monitoring, a series of experiments were conducted using real-world thermal images captured from substations. The dataset included 300 thermal images (resolution: 320×240) representing various electrical components under different operating conditions. The model was deployed and benchmarked on an NVIDIA Jetson Xavier NX edge computing platform. Each image was processed individually, and latency was recorded over 100 iterations to obtain an average runtime value. Power consumption and CPU/GPU utilization were also monitored during execution. The experimental results demonstrate that the proposed AI-based thermal image classification model achieves real-time inference capability when deployed on an embedded edge computing device. With an average processing speed exceeding 23 FPS during execution. The experimental results demonstrate that the proposed AI-based thermal image classification model achieves

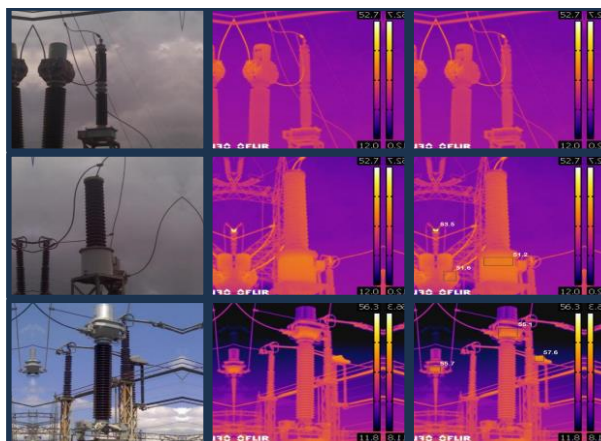


Figure 5. Temperature estimation on thermal image dataset (Doutorado, 2023)

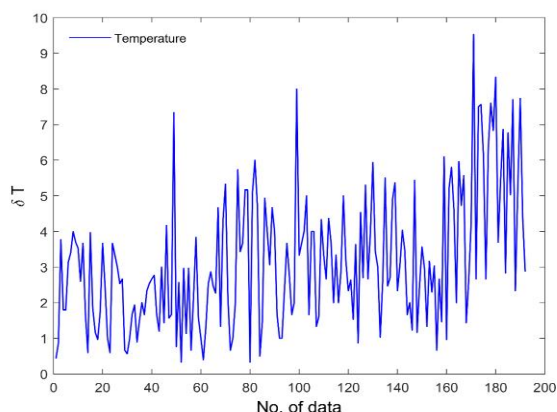


Figure 6. The difference between measured and extracted temperature

real-time inference capability when deployed on an embedded edge computing device. With an average processing speed exceeding 23 FPS and modest resource consumption, the system is well-suited for continuous monitoring and anomaly detection in electrical substations. The lightweight model architecture ensures compatibility with power-constrained field devices, supporting scalable and autonomous condition-based maintenance strategies in smart grid applications.

Despite the promising results, the proposed approach exhibits several limitations when deployed in real-world scenarios. First, environmental factors such as high reflectivity of metallic surfaces, inconsistent ambient lighting, and varying emissivity across different equipment types may lead to inaccurate thermal readings or misclassification. Second, preliminary experiments show a slight degradation in model performance under severe occlusion, partial obstruction of equipment, or when thermal contrast between faulty and healthy components are minimal. Additionally, the current dataset does not fully capture all possible variations in operational and environmental conditions, which may limit generalization. To address these challenges, ongoing research focuses on: enhancing adaptive image preprocessing techniques to normalize thermal contrast; applying domain-specific data augmentation to simulate noise and artifacts; exploring multi-modal fusion, combining thermal images with visible-spectrum data or electrical measurements to improve robustness. These efforts propose to increase the reliability and adaptability

of the system for real-time fault detection and diagnostics in complex electrical infrastructure.

Conclusions

This paper presents an efficient fault diagnosis method for electrical equipment based on infrared thermography, consisting of three key stages: image processing, temperature segmentation, and image feature analysis. The proposed OTS-based segmentation algorithm achieves a precision rate of 97.5%, outperforming the traditional Otsu method (96.31%) by effectively minimizing over-segmentation and improving hotspot localization. Furthermore, the spatial-temporal modeling technique enables accurate tracking of temperature variations, yielding a temperature estimation accuracy of 95.3%, with over 92.0% of measured points showing a deviation of less than 5°C compared to ground truth. Beyond numerical performance, the proposed method demonstrates high potential for real-time, non-contact thermal monitoring in substations and critical power infrastructure. Its lightweight nature makes it well-suited for edge deployment, supporting early fault detection and predictive maintenance. However, limitations exist when dealing with low thermal contrast, reflections from metallic surfaces, or environmental disturbances, which may introduce noise or false positives. To address these challenges, future work will focus on integrating multi-modal data (e.g., combining thermal and visible-spectrum images), improving robustness under real-world

noise, and benchmarking against advanced deep learning segmentation models. The method also creates promising applications in autonomous drone-based inspections and large-scale smart grid monitoring.

Acknowledgements

This research is funded by the Vietnam National University of Agriculture (VNUA) under grant number: TĐ2023.

References

- Ahmed M. M., Huda A. N. & Isa N. A. M. (2015). Recursive construction of output-context fuzzy systems for the condition monitoring of electrical hotspots based on infrared thermography. *Engineering Applications of Artificial Intelligence*. 39: 120-131. DOI: 10.1016/j.engappai.2014.11.010.
- Baba A. (2022). A new design of a flying robot, with advanced computer vision techniques to perform self-maintenance of smart grids. *Journal of King Saud University-Computer and Information Sciences*. 34: 2252-2261. DOI: 10.1016/j.jksuci.2020.07.009.
- Balakrishnan G. K., Yaw C. T., Koh S. P., Abedin T., Raj A. A., Tiong S. K. & Chen C. P. (2022). A review of infrared thermography for condition-based monitoring in electrical energy: Applications and recommendations. *Energies*. 15(16): 6000. DOI: 10.3390/en15166000.
- Bagavathiappan S., Lahiri B. B., Saravanan T., Philip J. & Jayakumar T. (2013). Infrared thermography for condition monitoring—a review. *Infrared Physics & Technology*. 60: 35-55. DOI: 10.1016/j.infrared.2013.03.006.
- Coutin M., Plumecocq W., Melis S. & Audouin L. (2012). Energy balance in a confined fire compartment to assess the heat release rate of an electrical cabinet fire. *Fire Safety Journal*. 52: 34-45. DOI: 10.1016/j.firesaf.2012.05.002.
- Doutorado R. (2023). Rna eduardo tese dataset. Retrieved from <https://universe.roboflow.com/rna-doutorado/rna-eduardo-tese>, aug 2023, visited on September 15, 2024.
- Doshvarpassand S., Wu C. & Wang X. (2019). An overview of corrosion defect characterization using active infrared thermography. *Infrared Physics and Technology*. 96: 366-389. DOI: 10.1016/j.infrared.2018.12.006.
- Fadzail N. F., Zali S. M., Khairudin, M. A. & Hanafi, N. H., (2020). Stator winding fault detection of induction generator based wind turbine using ANN. *Indonesian Journal of Electrical Engineering and Computer Science*. 19: 2502-4752. DOI: 10.11591/ijeecs.v19.i1.pp126-133.
- Fatima M. (2025). Intelligent active and reactive power control using multi-layer neural network based MPPT controller for grid tied solar PV system under fault conditions. *Indonesian Journal of Electrical Engineering and Computer Science*. 37: 2502-4752. DOI:10.11591/ijeecs.v37.i1.pp1-14.
- Huda A. & Taib S. (2013). Suitable features selection for monitoring thermal condition of electrical equipment using infrared thermography. *Infrared Physics and Technology*. 61: 184-191. DOI: 10.1016/j.infrared.2013.04.012.
- Jabbar F. I., Soomro D. M., Abdullah M. N., Radzi N. H. M., Baloch M. H., Rahmoon A. A. & Fakhrudden H. F. (2023). Optimize single line to ground fault detection in distribution grid power system using artificial bee colony. *Indonesian Journal of Electrical Engineering and Computer Science*. 31: 2502-4752, DOI: 10.11591/ijeecs.v31.i3.pp1286-1294.
- Jadin M. S. & Taib S. (2012). Recent progress in diagnosing the reliability of electrical equipment by using infrared thermography. *Infrared Physics and Technology*. 55: 236-245. DOI: 10.1016/j.infrared.2012.03.002.
- Jaffery Z. A. & Dubey A. K. (2014). Design of early fault detection technique for electrical assets using infrared thermograms. *International Journal of Electrical Power and Energy Systems*. 63: 753-759. DOI:10.1016/ijepes.2014.6.049.
- Kregg M. A. (2004). Benefits of using infrared thermography in utility substations. *Thermosense XXVI*, 5405. SPIE: 249-257. DOI:10.1117/12.549848.
- Luo Q., Gao B., Woo W. L. & Yang Y. (2019). Temporal and spatial deep learning network for infrared thermal defect detection. *Ndt & E International*. 108: 102164. DOI:10.1016/j.ndteint.2019.102164.
- Market S. (2025). LMD-based fault detection scheme for TCSC compensated wind integrated transmission lines. *Indonesian Journal of Electrical Engineering and Computer Science*. 37: 2502-4752, DOI: 10.11591/ijeecs.v37.i1.pp26-34.
- Nehete L., Bankar S., Asati R. & Khadse C. (2024). Non-contact power system fault diagnosis: a machine learning approach with electromagnetic current sensing. *Indonesian Journal of Electrical Engineering and Computer Science*. 36(3): 1356-1364. DOI: 10.11591/ijeecs.v36.i3.pp1356-1364.
- Ostu N. (1979). A threshold selection method from grey level histograms. *IEEE Trans SMC*. 9: 62.
- Pandurangan K. & Nagappan K. (2024). Hybrid total variance void-based noise removal in infrared images. *Indonesian Journal of Electrical Engineering and Computer Science*. 36: 1365-1378. DOI: 10.11591/ijeecs.v36.i3.pp1365-1378.
- Sedighi AR., Kafiri A., Sehhati MR. & Behdad F. (2020). Life estimation of distribution transformers using thermography: A case study Measurement. 149: 106-994.
- Xia C., Ren M., Wang B., Dong M., Xu G., Xie J. & Zhang C. (2021). Infrared thermography-based diagnostics on power equipment: State-of-the-art. *High Voltage*. 6: 387-407. DOI: 10.1049/hve2.12023.
- Xu X., Xu S., Jin L. & Song E. (2011). Characteristic analysis of otsu threshold and its applications. *Pattern Recognition Letters*. 32: 956-961.
- Ukrit K., Sansak D. & Saktanong W (2024). Safety hysteresis comparator design for transient overvoltage detection. *Indonesian Journal of Electrical Engineering and Computer Science*. 34(1): 2502-4752, DOI: 10.11591/ijeecs.v34.i1.pp69-80.
- Zhou D. & Xia Z. (2016). An improved otsu threshold segmentation algorithm. *textslJournal of the China University of Metrology*. 3: 319-323.
- Zou H. & Huang F. (2015). A novel intelligent fault diagnosis method for electrical equipment using infrared thermography. *Infrared Physics and Technology*. 73: 29-35. DOI: /10.1016/j.infrared.2015.08.019.